

Unions with UNIONS: Using galaxy-galaxy lensing to probe galaxy mergers

Isaac Cheng^{1,2*}, Jack Elvin-Poole^{1,3†}, Michael J. Hudson^{1,3,4‡}, Ruxin Barré^{5,1}, Sara L. Ellison⁵, Robert W. Bickley⁵, Thomas J. L. de Boer⁶, Sébastien Fabbro⁷, Leonardo Ferreira⁵, Sacha Guerrini⁸, Hendrik Hildebrandt⁹, Martin Kilbinger⁸, Alan W. McConnachie⁷, Ludovic van Waerbeke¹⁰ and Anna Wittje⁹

¹Department of Physics and Astronomy, University of Waterloo, 200 University Ave W, Waterloo, ON N2L 3G1, Canada

²Cahill Center for Astronomy and Astrophysics, California Institute of Technology, MC 249-17, Pasadena, CA 91125, USA

³Waterloo Centre for Astrophysics, University of Waterloo, 200 University Ave W, Waterloo, ON N2L 3G1, Canada

⁴Perimeter Institute for Theoretical Physics, 31 Caroline St. North, Waterloo, ON N2L 2Y5, Canada

⁵School of Physics and Astronomy, University of Victoria, Victoria, BC, Canada

⁶Institute for Astronomy, University of Hawaii, 2680 Woodlawn Drive, Honolulu HI 96822

⁷National Research Council of Canada, Herzberg Astronomy & Astrophysics Research Centre, 5071 West Saanich Road, Victoria, BC V9E 2E7, Canada

⁸Université Paris Cité, Université Paris-Saclay, CEA, CNRS, AIM, 91191, Gif-sur-Yvette, France

⁹Ruhr University Bochum, Faculty of Physics and Astronomy, Astronomical Institute (AIRUB), German Centre for Cosmological Lensing, 44780 Bochum, Germany

¹⁰Department of Physics and Astronomy, University of British Columbia, Vancouver, BC, V6T 1Z1, Canada

Accepted XXX. Received YYY; in original form ZZZ

ABSTRACT

We use galaxy-galaxy lensing to investigate how the dark matter (DM) haloes and stellar content of galaxies with $0.012 \leq z \leq 0.32$ and $10 \leq \log_{10}(M_{\star}/M_{\odot}) \leq 12$ change as a result of the merger process. To this end, we construct two samples of galaxies obtained from the Ultraviolet Near Infrared Optical Northern Survey (UNIONS), comprising 1 623 post-mergers and $\sim 30\,000$ non-merging controls, that live in low-density environments to use as our lenses. These samples are weighted to share the same distributions of stellar mass, redshift, and geometric mean distance to a galaxy’s three nearest neighbours to ensure differences in the lensing signal are due to the merger process itself. We do not detect a significant difference in the excess surface density profile of post-mergers and non-merging controls with current data. Fitting haloes composed of a point-like stellar mass component and an extended DM structure described by a Navarro-Frenk-White profile to the lensing measurements yields, for both samples, halo masses of $M_{\text{halo}} \sim 4 \times 10^{12} M_{\odot}$ and a moderately negative correlation between M_{halo} and concentration c . While the concentration of the post-mergers ($c = 0.76^{+1.04}_{-0.52}$) is lower than that of the controls ($c = 3.74^{+0.39}_{-0.34}$), the difference is not statistically significant at the 95 per cent confidence level. Both are somewhat lower than those predicted from simulations, possibly due to stronger feedback in nature than has been simulated and/or limitations of our fitted model. Furthermore, the stellar-to-halo-mass ratio of post-mergers is consistent with that of the controls, suggesting that galaxy mergers do not greatly affect the proportion of stellar mass relative to DM mass in post-mergers. Extreme merger-induced starbursts, in which more than 60 percent of the stars are formed in the burst, are ruled out at the 95 per cent confidence level. Although we do not find merger-induced differences in the DM haloes and stellar content of galaxies with our current data, application of our methods to upcoming surveys that are able to provide samples $\sim 10\times$ larger than our current catalogue are expected to detect the weak-lensing signatures of mergers and further constrain their properties.

Key words: gravitational lensing: weak – galaxies: evolution – galaxies: haloes

1 INTRODUCTION

Amongst the various drivers of galaxy evolution, perhaps the most spectacular is the rapid transformation of a galaxy’s physical and morphological properties due to galaxy mergers (e.g. via tidal forces, mass growth, gas flows, etc.). On longer timescales, in-situ star

formation (SF) gradually alters galaxies by creating, expelling, and reconstituting new elements, forming the great diversity of galaxy properties and stellar populations seen today. These two mechanisms are not independent, however. Galaxy mergers are known to trigger bursts of SF (e.g. Duc et al. 1997; Sanders et al. 1988; Jogee et al. 2009; Ellison et al. 2013), but they can equally quench SF on short timescales (e.g. Ellison et al. 2022; Davies et al. 2022; Ellison et al. 2024; Kado-Fong et al. 2024). The interplay of these two processes complicates our understanding of the long-term effects that mergers may have on SF in galaxies.

* E-mail: icheng@astro.caltech.edu, isaac.cheng.ca@gmail.com (IC)

† E-mail: jack.elvin-poole@uwaterloo.ca, jack.elvinpoole@gmail.com (JE-P)

‡ E-mail: mike.hudson@uwaterloo.ca (MJH)

While star formation rates (SFRs) in mergers are widely studied (e.g. Robaina et al. 2009; Ellison et al. 2013; Knäpen et al. 2015; Moreno et al. 2019; Pearson et al. 2019b; Shah et al. 2022), the total stellar mass produced as a result of merging is harder to probe since it requires integrating SFRs over many dynamical times, and is thus less well-understood. Recent results from Reeves & Hudson (2024) and Ferreira et al. (2025), each using different techniques, both show that the SF triggered by the merger process is responsible for 10–20 per cent of the post-merger galaxy’s stellar mass. This, in turn, changes the stellar-to-halo-mass ratio (SHMR) of the post-merger. Thus, measuring a galaxy’s SHMR is another way to understand how many stars could have formed in a merger-induced starburst. To demonstrate this, we consider the simple case of a merger between two galaxies sharing equal halo (M_{halo}) and stellar (M_{\star}) masses, forming a new system with $M_{\star} \approx 10^{11} M_{\odot}$. Using the fits to the SHMR as a function of M_{\star} in Hudson et al. (2015), we see that if the merger was at $z = 0.15$ and was “dry” (i.e. no induced SF), it would have a SHMR ≈ 25 per cent higher than a non-merging galaxy of the same stellar mass. If, on the other hand, the merger triggers a ~ 20 per cent starburst (i.e., the fraction of stars formed due to merging is 20 per cent of the post-merger’s final stellar mass), the SHMR immediately after the burst would be ≈ 60 per cent higher than a galaxy of the same M_{\star} .

In addition to changing stellar mass and SHMR, galaxy interactions are also expected to change the mass density profile of merging systems and their products (Wang et al. 2020), which we can measure using the weak gravitational lensing signal of background galaxies around the positions of the mergers—that is, using galaxy-galaxy lensing. The mass profile of mergers can, of course, be studied using simulations (e.g. Springel et al. 2005; Hopkins et al. 2006), but simulating the baryonic content of galaxies is very computationally challenging while modelling a galaxy’s dark matter is much simpler. Conversely, it is impossible to observe the dark matter (DM) directly, whereas the baryonic matter is observable via electromagnetic radiation. Using galaxy-galaxy lensing, we can probe the DM content of observationally-identified mergers and thus act as a bridge between theory and observation.

Until recently, however, a sufficiently large catalogue of merger products was simply unavailable for the purposes of a weak lensing analysis. While pre-mergers (i.e. pairs that will soon merge or systems that have started merging but have not fully coalesced) are relatively easy to find based on just position and redshift (see e.g. Ellison et al. 2008; Domingue et al. 2009; Xu et al. 2012; Gonzalez et al. 2023), identification of post-mergers (i.e. systems that have fully coalesced after a merger) is much harder (Wilkinson et al. 2024) and manual inspection cannot keep up with the meteoric growth in astronomy data sizes. Fortunately, machine learning provides a promising avenue for automated merger identification using neural networks (NNs).

Historically, convolutional neural networks (CNNs) have been the NN of choice for identifying galaxy mergers due to their exceptional performance in image processing and analysis (e.g. Huertas-Company et al. 2015; Pearson et al. 2019a,b; Bickley et al. 2021; Rose et al. 2024). Recently, Ferreira et al. (2024) combined vision transformers (ViTs) with CNNs in a two-stage hierarchical merger identification framework, achieving post-merger purities $\gtrsim 95$ per cent even at ~ 1 Gyr after the merger event.

Motivated by the success of NNs in identifying mergers and the release of new, large catalogues of candidate mergers suitable for a weak lensing analysis, here we investigate how galaxy mergers change the DM structure and stellar content of galaxies using galaxy-galaxy lensing. Previously, the only instance that we know of that attempted to use galaxy-galaxy lensing to study galaxy mergers (albeit in the

context of mergers triggering black hole activity, for which they found a null result) is from Harvey & Courbin (2015), who looked at 29 post-starburst galaxies containing quasars whose SF histories indicated recent merger activity. In this work, we increase the sample size of post-mergers by a factor of ≈ 56 and we do not rely on the post-starburst signature to identify merger products, since post-starburst mergers comprise a minority of post-merger systems (Ellison et al. 2022 find $\lesssim 20$ per cent of post-mergers are also post-starbursts), meaning the properties of post-starburst galaxies may not be reflective of post-mergers as a whole.

Throughout this paper, we assume a flat Λ CDM cosmology with $H_0 = 70 \text{ km s}^{-1} \text{ Mpc}^{-1}$, $\Omega_{\text{m},0} = 0.3$, $\Omega_{\Lambda,0} = 0.7$, $\Omega_{\text{b},0} = 0.049$, $\sigma_8 = 0.81$, and $n_s = 0.95$. We outline the data used for our project in Section 2, followed by our methods in Section 3. We then present and discuss the results of our analysis in Section 4, and conclude in Section 5.

2 DATA

The data for our analysis include a catalogue from Ferreira et al. (2024) comprising galaxies at various stages in the merger sequence, and a source catalogue from the Ultraviolet Near Infrared Optical Northern Survey (UNIONS; Guinot et al. 2022; Farrens et al. 2022; Gwyn et al. in prep). UNIONS is a collaboration of wide-field imaging surveys of the northern hemisphere, consisting of the Canada-France Imaging Survey (CFIS) conducted at the 3.6 m Canada-France-Hawaii Telescope (CFHT) on Maunakea, members of the Pan-STARRS (Panoramic Survey Telescope and Rapid Response System) team, and the Wide Imaging with Subaru Hyper Suprime-Cam of the Euclid Sky (WISHES) team. CFHT/CFIS is obtaining deep imaging in the u - and r -bands, Pan-STARRS is obtaining deep i - and moderate-deep z -band imaging, and Subaru is obtaining deep imaging in the z -band through WISHES and g -band through the Waterloo-Hawaii Institute for Astronomy g -band Survey (WHIGS). In the following, we describe our two datasets in more detail.

2.1 Lens Galaxies

To study the DM haloes of galaxy mergers, we use the catalogue from Ferreira et al. (2024) that includes 235 354 galaxies at different stages in the merger sequence: pre-mergers/pairs, post-mergers, and non-mergers. The objects in this catalogue are composed of galaxies with spectroscopic data in the Sloan Digital Sky Survey (SDSS) Data Release 7 (DR7) that are additionally contained in the UNIONS CFIS Data Release 5 (DR5) survey area. We do not use the pre-mergers/pairs in our subsequent analysis because we do not expect them to be well-described by a single DM halo, and is thus beyond the scope of this paper.

Each galaxy in our catalogue has an SDSS DR7 object ID, (RA, Dec) on-sky coordinate, the vote count from each of the two MUMMI NN stages (described below), and a “merger class” designation indicating whether the galaxy is a non-merger, part of a pre-merger pair, or is a post-merger. We additionally use the object IDs to match galaxies to SDSS and MPA-JHU (Max Planck Institute for Astrophysics and Johns Hopkins University) catalogues to obtain, for each of the 184 485 galaxies in common across all three datasets, a spectroscopic redshift z from SDSS and a stellar mass estimate M_{\star} from MPA-JHU¹. The

¹ <https://wwwmpa.mpa-garching.mpg.de/SDSS/DR7/Data/stellarmass.html>

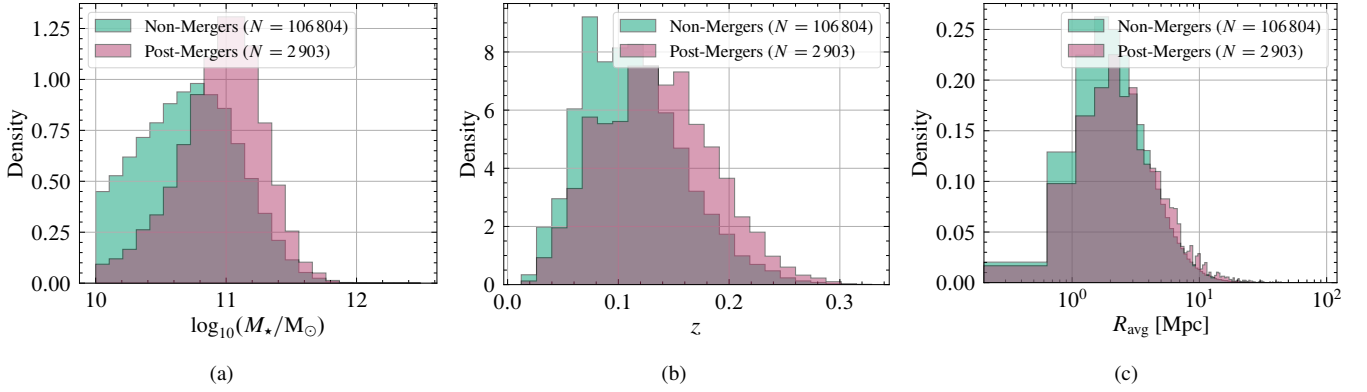


Figure 1. Raw distributions of various galaxy properties in our lens catalogue ($M_{\star} \geq 10^{10} M_{\odot}$), before matching sample properties. (a) The raw stellar mass distribution. (b) The raw redshift distribution. (c) The raw distribution of the geometric mean distance to each galaxy’s three nearest neighbours.

stellar masses are derived from SDSS *ugriz* photometry using the template models of Bruzual & Charlot (2003) assuming a Chabrier (2003) initial mass function².

Merger identification and merger stage classification are based on the values given by MUMMI (Ferreira et al. 2024), a novel NN ensemble composed of convolutional and vision transformer units. We summarize the NN training, architecture, and results below. The MUMMI training and validation data come from mock images of IllustrisTNG100-1 galaxies (Nelson et al. 2019) spanning $0.01 \leq z \leq 0.3$ and $10^{10} M_{\odot} \leq M_{\star} \leq 10^{11} M_{\odot}$ to generally replicate the morphologies seen in UNIONS. To generate these data, 17 894 pre-mergers and 21 485 post-mergers are selected from TNG100-1; the latter are galaxies whose progenitors have stellar mass ratios $\mu \geq 0.1$ and have merged in the last 1.7 Gyr, with no companions within 50 kpc. Each merger is matched in redshift, stellar mass, and gas fraction to a non-merging control from TNG100-1. A non-merger is a galaxy that has no merger event within 1.7 Gyr, both in the past and in the future (relative to its observed redshift). Non-mergers that could potentially merge in the future after the simulation ends have a minimum separation of 50 kpc so that they are unlikely to merge within the next Gyr (Patton et al. 2024). Then, for each galaxy, 80 mock UNIONS realizations are produced using REALSIMCFIS, a pipeline based on REALSIM³.

The 6 300 640 mock images are classified by MUMMI in a two-step process: first determining if a galaxy is a merger or non-merger, then separating the mergers into pre-mergers and post-mergers. Step 1 (merger identification) is accomplished with an ensemble of 20 NNs (10 pairs of CNNs and SwinTransformers), with a positive merger identification only if all 20 models agree. Step 2 (merger classification) uses a single CNN-SwinTransformer pair to determine the probability that the galaxy is a post-merger, with a “merger class” label of post-merger if the probability is greater than 50 per cent. This hierarchical approach leads to samples that are above 95 per cent purity for post-mergers that are observed within 1.25 Gyr of the merger event.

Finally, the trained MUMMI ensemble is applied to UNIONS/CFIS *r*-band cutouts with a 12 Petrosian radius field of view, giving

us 3 096 galaxies unanimously deemed to be post-mergers in the UNIONS/SDSS DR7/MPA-JHU overlap. These post-mergers are generally isolated and feature disturbed morphologies such as tidal tails and warped spiral arms (for more details, see Ferreira et al. 2024). The requirement of unanimity in MUMMI step 1 maximizes the purity of our post-merger sample. Likewise, to increase purity in the non-merging sample, a non-merging candidate may have no more than three votes classifying it as a merger in MUMMI step 1; if we simply classified non-mergers as those that do not have unanimous agreement in the first step, there will be many false positives such as a merging system that is correctly identified by (only) 19 of the 20 models. We note that, even with this scheme, it is possible that there is a small number of false positives among the 132 790 non-mergers, but the contaminating fraction should be small on account of the rarity of mergers in the Universe (see e.g. Casteels et al. 2014; Ferreira et al. 2024) and these missed mergers should be dominated by post- rather than pre-mergers. This is because pre-mergers, in contrast to post-mergers, are actually fairly easy to identify (see also the discussion in Section 1). Thus, there is little chance that a pre-merger only attains 3 votes or fewer in the first step of MUMMI, meaning any false positives in the non-merging sample are likely to be post-mergers. We note here that, as discussed in Ferreira et al. (2024), the MUMMI post-merger galaxies tend toward higher redshifts and stellar masses than the overall sample of galaxies in SDSS/UNIONS (see Fig. 1). In this work, we do not make any attempt to correct for this selection effect.

Lastly, we impose a minimum stellar mass of $10^{10} M_{\odot}$ in our samples to maximize the confidence in our galaxy classifications, as MUMMI is designed for galaxies above this stellar mass threshold⁴. In contrast, we do not need to apply additional redshift cuts since our samples (Fig. 1) naturally span a redshift range of $0.012 \leq z \leq 0.33$, which ensures our galaxies and any close neighbours fit within the 12 Petrosian radius field of view used by MUMMI and minimizes the chance that an unresolved point-like source, such as a quasar, is accidentally included in our sample (Ferreira et al. 2024). The addition of a stellar mass cut on our samples does not change any of the results presented in this paper; for reference, our M_{\star} cut reduces our final post-merger and non-merging control sample sizes (see Section 3) by 4 per cent and 6 per cent, respectively.

We show in Figs. 1a and 1b the distributions of stellar mass and redshift in our samples. In order to determine the environment of

² Note that these M_{\star} estimates are similar, but not identical to, those of Kauffmann et al. (2003), as stated in the MPA webpage linked in the previous footnote. For a more detailed comparison between the MPA-JHU stellar masses and those in Kauffmann et al. (2003), see https://www.mpa.mpa-garching.mpg.de/SDSS/DR7/mass_comp.html.

³ <https://github.com/cbottrell/RealSim>

⁴ Note, however, that MUMMI classifications should generalize to stellar masses outside of its training range (Ferreira et al. 2024, section 4.4). As we discuss in the text, our results are robust to this M_{\star} cut.

the lenses, we also convert the on-sky coordinates of each galaxy into a three-dimensional position using its spectroscopic redshift and the cosmology given in Section 1, assuming the galaxies follow the Hubble flow without any peculiar velocities. We then calculate the distance to each galaxy’s three nearest neighbours⁵ and compute the geometric mean of these three separations, which we call R_{avg} ; we use these values in Section 3.1. Fig. 1c shows the resulting R_{avg} distribution.

2.2 Background Source Galaxies

The shapes of the background source galaxies come from the UNIONS ShapePipe v1.3 catalogue, a collection of ~ 84 million galaxies with shape measurements derived from CFIS r -band data. These sources are stacked in annuli around each of our lenses to perform the tangential shear measurement described in Section 3.4. In the following, we provide a brief overview of the shape measurement pipeline (Guinot et al. 2022; Farrens et al. 2022) including v1.3 improvements (Li et al. 2024).

Objects, including both point-like and extended sources, are initially extracted from stacked r -band CFIS images using SOURCEEXTRACTOR (Bertin & Arnouts 1996) with a 1.5σ detection threshold. The minimum area to detect an object in v1.3 has been changed from 10 to 3 pixels to reduce galaxy selection bias in the resulting shear estimates. Next, to differentiate between point sources and galaxies, each object is compared to a “spread model” (Desai et al. 2012; Mohr et al. 2012) consisting of a point source profile and an extended profile. An object is considered a galaxy if its spread model is greater than zero while satisfying a number of other cuts based on the model uncertainty, object magnitude, size of the extended source relative to the size of the point spread function (PSF), and the relative error in the flux. In v1.3, estimates of the PSF are obtained using multi-CCD (MCCD) modelling (Liaudat et al. 2021) instead of PSFEx (Bertin 2011). The MCCD approach gives a simultaneous non-parametric estimate of the PSF across all CCDs to better capture PSF variations over the whole field of view. Moreover, the size of the galaxy (T_{gal}) relative to the PSF (T_{PSF}) has an additional constraint in v1.3 to reject diffuse, low signal-to-noise artifacts in the image: $T_{\text{gal}}/T_{\text{PSF}} < 3$. Lastly, galaxy shapes are measured using NGMIX⁶ and calibrated using the metacalibration method (Huff & Mandelbaum 2017; Zuntz et al. 2018).

Notably, there are no spectroscopic redshifts for these sources at present, but the effective redshift distribution $n(z_s)$ for the photometric sample is estimated from colour space based on the method from Wright et al. (2020). The process applied to UNIONS is described in Li et al. (2024, appendix A) and we summarize it here. The sources are first cross-matched to the CFHTLenS (Canada-France-Hawaii Telescope Lensing Survey, Heymans et al. 2012) W3 field and assigned $ugriz$ magnitudes (Hildebrandt et al. 2012). These magnitudes and colours are input to a self-organizing map (SOM, Kohonen 1982) to reduce their multi-dimensional space to a 2D plane. A sample of galaxies with the same photometry and spectra from external surveys are also input to the SOM as a calibration dataset, and their redshift distribution is weighted such that it matches that of the total source sample, based on the lensing weights and the number density per SOM region. The resulting weighted distribution is then used as an estimate of the photometric sample’s $n(z_s)$, as shown in Figure

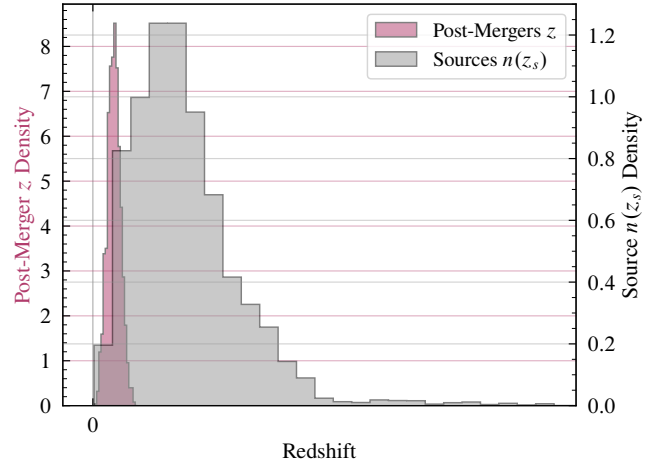


Figure 2. The effective redshift distribution of the sources, $n(z_s)$, compared to the post-merger spectroscopic redshift distribution from Fig. 4b. For cosmology calculations the $n(z_s)$ redshifts are still blinded, but for reference, the average post-merger redshift is around $\langle z \rangle \approx 0.15$.

2. This $n(z_s)$ distribution is used to calculate the effective critical surface density, described in Section 3.4.

As a final note, the ShapePipe v1.3 catalogue does not have an estimate for the scalar bias needed to compute a shear bias correction to our lensing measurements in Section 3.4. However, since the bias affects lensing amplitudes by just a few per cent, it is accounted for in our uncertainties, which are all substantially larger (see Section 4).

3 METHODS

We now describe the procedure for our weak lensing analysis. We prepare our lenses (i.e. the post-mergers as well as the non-merging galaxies from which we will select our controls) for lensing measurements in Sections 3.1 and 3.2 by ensuring their redshift and stellar mass distributions match, as well as by controlling our sample so that the galaxies all live in similar, low-density environments. We always match our distributions to the post-merger sample, since that is our smallest dataset and we do not want to further reduce its effective size. These preprocessing steps are important because they ensure that we are measuring differences in the lensing signal caused by the merger process, as opposed to differences caused by sampling separate galaxy populations with distinct, merger-unrelated properties or environments.

In addition to matching the lens samples’ M_* , z , and R_{avg} distributions, we also construct a set of random lenses in Section 3.3 that we use for various lensing correction factors. Section 3.4, in turn, describes the computational method by which we perform the lensing measurements. Finally, Section 3.5 details the procedure for fitting DM haloes to the lensing signal.

3.1 Environment Control

We begin by preferentially choosing lenses that live in low-density environments to mitigate the need to model the correlation between our lens galaxies and neighbouring haloes (the so-called 2-halo term, see e.g. Cooray & Sheth 2002). This also ensures that the post- and non-merger lens samples contain galaxies that all live in similar environments.

⁵ Nearest in three-dimensional space, not nearest in projected 2D on-sky separation.

⁶ <https://github.com/esheldon/ngmix>

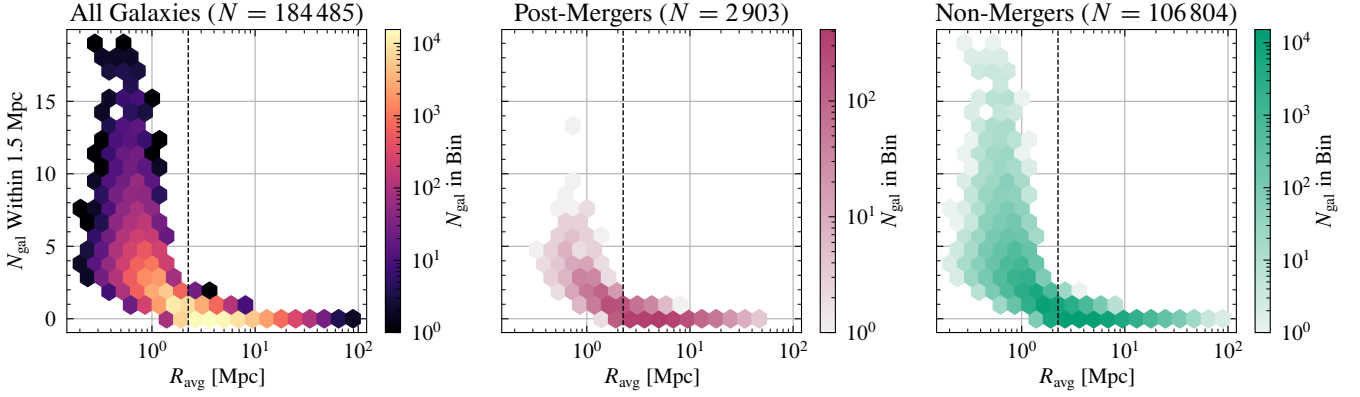


Figure 3. 2D hexbin plots showing our metrics for environment density: the number of neighbouring galaxies within 1.5 Mpc and the geometric mean distance to the three nearest neighbours of each galaxy, R_{avg} . The colouring represents the number of galaxies, N_{gal} , in a hexbin. The vertical dashed line indicates $R_{\text{avg}} = 2.25$ Mpc. We want to select galaxies that live in low-density environments (i.e. the bottom right region of these plots).

We determine the extent to which a galaxy is isolated using two metrics: the number of other galaxies within a distance of 1.5 Mpc (i.e. the upper limit of our radial bins in our lensing measurements, see Section 3.4), and the geometric mean distance to a galaxy’s three nearest neighbours. Distances are calculated from a galaxy’s spectroscopic redshift converted into Cartesian coordinates using its on-sky location and angular diameter distance, assuming the cosmology from Section 1 and neglecting possible peculiar velocities on top of the Hubble flow. To compute these metrics, we simply search within the catalogue of 184 485 galaxies described in Section 2.1 as these data come from a complete sample of spectroscopic redshifts and alternative samples would not have full overlap with our footprint. Note that these searches consider *all* galaxies in the catalogue including pre-mergers and galaxies with $M_{\star} < 10^{10} M_{\odot}$, not just the post-mergers and non-mergers that we use.

Since we are using spectroscopic redshifts from SDSS DR7, there may be neighbouring galaxies that are missed in these searches due to fibre collisions. These fibre collisions are an instrument limitation where the fibres on the spectrographic plates used by SDSS cannot be placed closer than $55''$ (Strauss et al. 2002); galaxies closer than $55''$ in separation are selected at random⁷ to be observed spectroscopically (Strauss et al. 2002). Although only ~ 6 per cent of galaxies in SDSS lack spectra due to the physical limitations of fibre placement (Strauss et al. 2002; Tago et al. 2010), Patton & Atfield (2008) find that $\lesssim 30$ per cent of pairs with projected angular separation $< 55''$ have spectroscopic redshifts for both galaxies⁸. However, MUMMI results show that the unanimous post-mergers in UNIONS/CFIS are generally isolated galaxies (Ferreira et al. 2024), so our samples (after matching the non-mergers to the post-mergers in Section 3.2) should indeed live in relatively low-density environments. Furthermore, while having a low-density environment makes modelling DM haloes simpler, it is not necessary for our lensing measurements, which only require that the galaxy samples live in the *same* environment—this we achieve with our strategy presented below.

Two-dimensional histograms of our two environmental density

metrics are shown in Fig. 3. To select lenses that live in low-density environments, we choose galaxies with no companions within 1.5 Mpc. Additionally, we also require that the average distance to a galaxy’s three nearest neighbours, R_{avg} , be greater than 1.5×1.5 Mpc. This is because the centres of some neighbouring galaxies may be just outside the 1.5 Mpc search radius, rendering them invisible to our first metric, but the DM haloes of these neighbouring galaxies will still influence lensing amplitudes in the upper radial bin ending at 1.5 Mpc. Hence, we conservatively require the minimum R_{avg} to be greater than 2.25 Mpc.

3.2 Weighting of Lenses

After rejecting galaxies that do not meet the two conditions in Section 3.1, we fit three-dimensional kernel density estimates (KDEs) to the resulting samples’ joint M_{\star} - z - R_{avg} distributions (i.e. one joint distribution for post-mergers and one joint distribution for non-mergers). The KDEs are used to assign weights to the non-merger sample according to the formula:

$$w = \frac{f_{\text{post}}(M_{\star}, z, R_{\text{avg}})}{f_{\text{non}}(M_{\star}, z, R_{\text{avg}})}, \quad (1)$$

where w is the weight given to a non-merging galaxy, f_{post} and f_{non} are the post- and non-merger KDEs, and the M_{\star} , z , R_{avg} values refer to the sample being weighted (i.e. the non-mergers). These weights ensure the distributions between our two samples are the same, as seen in Fig. 4. In this way, we have constructed a non-merging control sample that is matched to the post-mergers. Two-sample Kolmogorov-Smirnov (KS) tests performed on the distributions verify that the post-mergers and controls have similar properties (p -values of 0.38, 0.35, 0.34 for the stellar mass, redshift, and R_{avg} distributions, respectively).

Note that we choose to fit KDEs to the data instead of directly assigning weights from histogram bins because histograms can be very jagged, but we expect the underlying distributions of M_{\star} , z , and R_{avg} to be smooth and continuous⁹. Thus, fitting KDEs to the

⁷ Since all galaxies, excluding those hosting candidate quasars, have equal priority in the SDSS spectroscopic target selection (see Strauss et al. 2002, section 4.5).

⁸ This 30 per cent completeness number also includes false pairs that are only close in projection. The completeness fraction for true pairs (i.e. those close in 3D space) with spec- z relative to all true pairs should be higher.

⁹ Depending on the histogram binning, galaxies on the edge of two bins could drastically change their weight just by falling into a different bin. This will not happen with KDEs since they are continuous distributions where small changes in inputs lead to small changes in outputs.

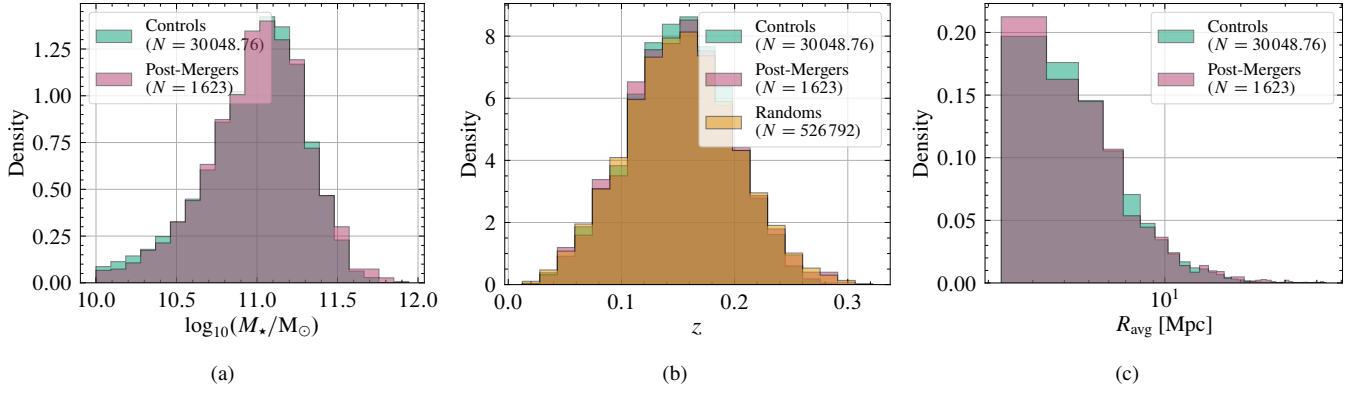


Figure 4. The weighted distributions of our final lens samples’ galaxy properties. These galaxies are selected to live in low-density environments, as discussed in the text, and matched in (a) stellar mass, (b) redshift, and (c) the geometric mean distance to their three nearest neighbours. Two-sample KS test p -values for the controls and post-mergers are: (a) 0.38, (b) 0.35, and (c) 0.34, indicating that differences in these weighted samples are not statistically significant. The redshifts of the randoms come from directly sampling the post-merger’s redshift KDE; a KS test between these two distributions yields $p = 0.80$.

data allows us to obtain smoothly varying weights over continuous intervals.

The final effective sample sizes are: 1 623 post-mergers and about 30 000 non-merging controls. An effective sample size (ESS) accounts for possibly unequal weighting of data and is calculated as (Kish 1992, equation (4.3)):

$$\text{ESS} = \frac{(\sum_i w_i)^2}{\sum_i w_i^2}, \quad (2)$$

where w_i are the weights of the galaxies in a given sample ($w_i = 1$ for all post-mergers) and the sums run over the entire sample. When all weights are equal, the ESS is equal to the actual sample size, but the ESS decreases as weights become more concentrated in fewer data points.

3.3 Construction of Randoms

In addition to the photometric redshift correction $n(z_s)$ mentioned in Section 2.2, we also construct a random catalogue of lenses to correct for two other effects: lensing systematics (corrected via random subtraction), and an overabundance of unlensed sources that are physically near lenses, causing the lensing amplitude to be underestimated (corrected via the boost factor).

To create our randoms catalogue, we generate $\sim 10\times$ more random lenses than true lenses¹⁰ uniformly within the true lenses’ footprint—namely, the overlapping region between the SDSS DR7 footprint and the currently-surveyed area by UNIONS. We determine the intersection of these two surveys using the SDSS DR7 spectroscopic coverage table¹¹, which contains the pointings for the 3° -diameter plate centres, and a list of UNIONS footprint tiles each covering an area of $0.5^\circ \times 0.5^\circ$. The spatial distributions of our true lenses and random lenses are shown in Fig. 5, covering an area of 1 995 square degrees.

We match the redshift distribution of our randoms to the post-mergers by randomly assigning redshifts sampled from a KDE fitted to the post-mergers’ z -distribution. Fig. 4b shows the redshift distributions of our various lens samples, including the randoms catalogue.

¹⁰ The ESS of the random lenses, which are equally weighted, happens to be $\sim 17\times$ that of the true lenses.

¹¹ <https://classic.sdss.org/dr7/coverage/maindr72spectro.par>

3.4 $\Delta\Sigma$ Measurements

After pre-processing the data as described above, we measure their lensing amplitudes using the `DSIGMA` Python package (Lange & Huang 2022). Briefly, `DSIGMA` measures the excess surface density $\Delta\Sigma$ around our lenses, defined as the mean surface density within a circle of projected radius R minus the mean surface density at the edge of a circle of projected radius R :

$$\Delta\Sigma(R) = \overline{\Sigma(<R)} - \langle\Sigma(R)\rangle. \quad (3)$$

It accomplishes this by binning and stacking background source galaxies in annuli around each of our (possibly weighted) lenses and measuring the overall tangential shear, $\langle\gamma_t\rangle$, of the stacked sources. This measurement of $\langle\gamma_t\rangle$ is a proxy for $\Delta\Sigma$ via the relation:

$$\langle\gamma_t\rangle = \Sigma_{\text{crit}}^{-1} \Delta\Sigma(R), \quad (4)$$

given a cosmology.

We improve the $\Delta\Sigma$ measurement of equation (4) by including the boost factor and random subtraction, so the full estimator of excess surface density becomes (Lange & Huang 2022):

$$\Delta\Sigma(R) = b(R)\Delta\Sigma_{\text{true lens}}(R) - \Delta\Sigma_{\text{random lens}}(R). \quad (5)$$

Here, $\Delta\Sigma_{\text{true/random lens}}$ is the lensing signal calculated around the true/random lenses, and

$$b(R) = \frac{\sum_{l-s} w_{\text{sys},l} w_{l-s}}{\sum_{r-s} w_{\text{sys},r} w_{r-s}} \quad (6)$$

is the radially-dependent boost factor. \sum_{l-s} and \sum_{r-s} denote that the sum goes over each lens-source and random-source pair. $w_{\text{sys},l}$ and $w_{\text{sys},r}$ are the weights for the true lenses and random lenses; these are equal to the weights in equation (1) for controls and equal to 1.0 for the post-mergers and randoms. Furthermore, w_{l-s} and w_{r-s} are weights to minimize shape noise in our stacked signal, calculated using:

$$w_{l-s/r-s} = w_s \Sigma_{\text{crit}}^{-2}(z), \quad (7)$$

where w_s is the inverse variance weight for the galaxy shape in our source catalogue and z is the redshift of the true/random lens.

Note that in formulas above, $\Sigma_{\text{crit}}^{-1}$ refers to the photo- z corrected (inverse) critical surface density:

$$\Sigma_{\text{crit}}^{-1}(z) = \int \tilde{\Sigma}_{\text{crit}}^{-1}(z, z_s) n(z_s) dz_s, \quad (8)$$

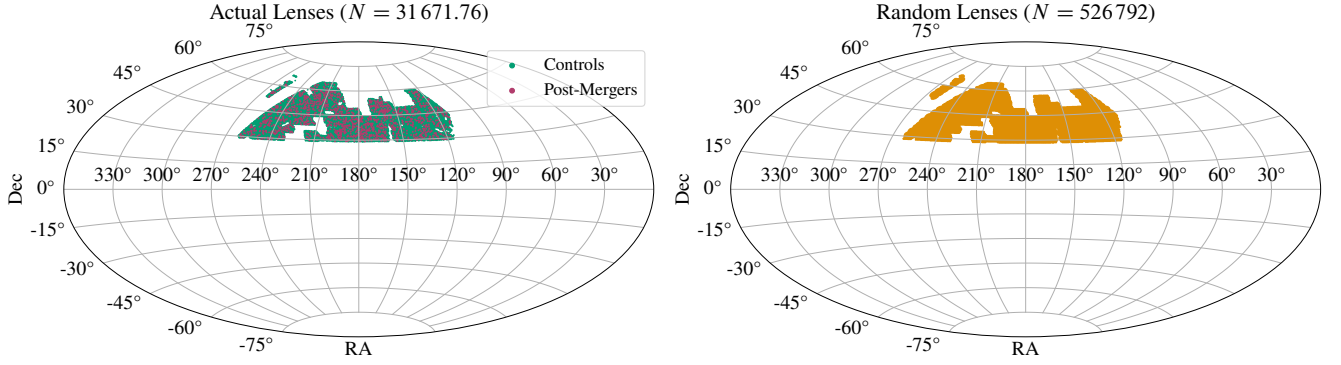


Figure 5. Sky coverage of the true lenses (*left*) and random lenses (*right*).

where $n(z_s)$ is the distribution from Section 2.2 and

$$\tilde{\Sigma}_{\text{crit}}^{-1}(z, z_s) = \frac{4\pi G}{c^2} \frac{D_A(z)D_A(z, z_s)}{D_A(z_s)} \quad (9)$$

is the standard (inverse) critical surface density that is dependent only on angular diameter distances—that is, only dependent on the geometry—between observer and lens, $D_A(z)$, observer and source, $D_A(z_s)$, and between lens and source, $D_A(z, z_s)$.

Lastly, the uncertainties in the measured $\Delta\Sigma$ signal come from jackknifing $N_{\text{JK}} = 100$ different patches of the sky, which accounts for physically correlated noise (e.g. due to foreground large-scale structures). Any uncertainties that arise from our various correction factors are propagated through to the final $\Delta\Sigma$ uncertainty since the jackknife error estimate is determined after all corrections are applied.

These $\Delta\Sigma$ measurements are performed in $N_b = 14$ linearly-spaced radial bins of equal width spanning $R = 0.1$ Mpc to $R = 1.5$ Mpc. The upper limit of $R = 1.5$ Mpc should be sufficiently large to enclose the DM haloes of our galaxies, which have stellar masses of $\sim 10^{11} M_\odot$. The lower limit of $R = 0.1$ Mpc is to avoid biases that arise when shape measurements are made too close to the centre of lenses.

3.5 Fitting Halo Profiles

Finally, we fit Navarro-Frenk-White (NFW) profiles to the $\Delta\Sigma$ measurements to determine whether the merger process produces measurable differences in the DM haloes of galaxies. In our analysis, we adopt a virial overdensity threshold that varies with redshift as given by Bryan & Norman (1998) and implemented in the `colossus` Python package (Diemer 2018). For our lenses, which have an average redshift of $\langle z \rangle \approx 0.15$, this virial overdensity corresponds to $\sim 114\times$ the critical density of the Universe. This overdensity threshold defines the edge of our halo radius R_{vir} and therefore the enclosed halo mass M_{halo} and concentration c .

Our full model consists of two components: an NFW halo and a point-like mass of stars at the centre of the galaxy. The stellar component has a mass equal to the weighted arithmetic mean of the stellar masses in the given lens sample, with weights given by equation (1) for controls and unity weights for post-mergers. The DM component has two free parameters that we fit to the data: the halo mass and concentration. The small (< 2 per cent) uncertainties in the stellar masses estimated from 10 000 bootstrapping iterations justify our choice to keep M_\star as a fixed parameter (see Table 1 in Section 4), allowing for smaller uncertainties in the free parameters.

We find the best-fitting M_{halo} and c to our $\Delta\Sigma$ measurements using

a Markov chain Monte Carlo routine to minimize the following χ^2 :

$$\chi^2 = \left(\Delta\Sigma - \widehat{\Delta\Sigma} \right)^T \mathbf{C}^{-1} \left(\Delta\Sigma - \widehat{\Delta\Sigma} \right), \quad (10)$$

where $\Delta\Sigma$ is a vector containing our measurements from Section 3.4, $\widehat{\Delta\Sigma}$ is a vector containing the predicted $\Delta\Sigma$ amplitudes using the current parameters, and \mathbf{C}^{-1} is the unbiased inverse covariance matrix of our $\Delta\Sigma$ values accounting for the Hartlap factor (Hartlap et al. 2007). We adopt uninformed, uniform priors for the halo mass and concentration, where the log-prior probabilities are zero for $M_{\text{halo}} \geq 10^9 M_\odot$ and $0 \leq c \leq 10$, and negative infinity otherwise.

Note that in our analysis, we only model single NFW haloes without any additional contributions from other galaxies or from the environment (such as the underlying dark matter halo of a galaxy cluster). As discussed in Section 3.1, although the SDSS DR7 spectroscopic catalogue is extensive, our environment control procedure is imperfect because fibre collisions may cause undercounting of the number of neighbouring galaxies around a lens. Moreover, we estimate three-dimensional distances from redshift by assuming galaxies move only according to the Hubble flow. Galaxies in dense clusters with relatively large peculiar motions may therefore be mistaken to be far apart simply because we assume differences in redshift are entirely due to cosmological expansion. With these considerations, we only fit to data points below $R \leq 1.0$ Mpc, since beyond this distance, the 2-halo term becomes important (Cooray & Sheth 2002, fig. 11).

4 RESULTS AND DISCUSSION

We now present the results of our analysis detailed in Section 3. Fig. 6 shows the $\Delta\Sigma$ measurements using our lenses from Fig. 4. We remark that the largest boost correction increases $\Delta\Sigma$ by ~ 10 per cent in the smallest radial bin, gradually decreasing to corrections of less than 3.5 per cent for $R \in [1.4, 1.5]$ Mpc, in agreement with previous work (e.g. Prat et al. 2022, fig. 3, first column).

Additionally, Fig. 6 suggests that the lensing signal of the post-mergers is not significantly different from that of the controls. Indeed, we can perform a chi-square test to examine the null hypothesis that the $\Delta\Sigma$ profile from a given sample is *not* significantly different from that of another sample. For our $\chi^2_{1,2} = 14.50$, we obtain $p = 0.41$, i.e. post-mergers and controls do not produce significantly different lensing amplitudes. Note that comparing only the 9 data points where $R \leq 1.0$ Mpc does not appreciably change the p -value (which becomes $p = 0.34$).

Next, we fit an NFW halo to each of our datasets following the procedure given in Section 3.5. Fig. 7 shows the best-fitting

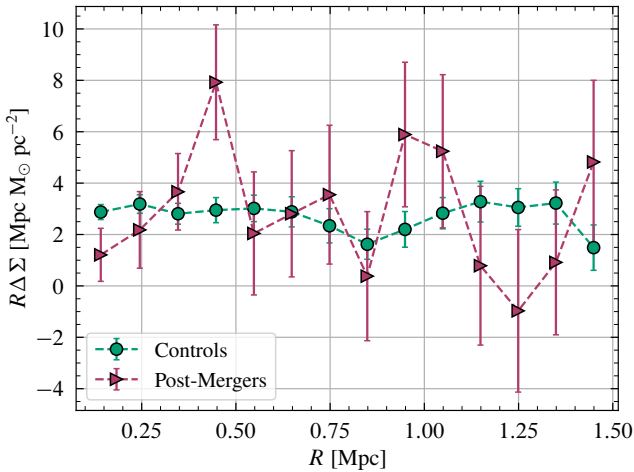


Figure 6. The $R\Delta\Sigma$ signal of our lenses (post-mergers and non-merging controls). R is the distance from the centre of the lens and $\Delta\Sigma$ is the excess surface density. The lensing amplitudes include boost correction and random subtraction.

models as well as constraints on—and correlations between—the fitted parameters. We check that the fitted models are actually *good* fits by performing a chi-square test and find that the data and model are mutually consistent. Our best-fitting parameters are summarized in Table 1.

Fig. 7 reveals that M_{halo} is moderately negatively correlated with c in the fits to both datasets. This is because decreasing the concentration pushes the mass out to larger radial scales; to keep the lensing signal the same (i.e. at small $R \leq 1.0$ Mpc), the halo mass must therefore increase to compensate for the lower concentration. We now examine each of these parameters in more detail.

At the 95 per cent confidence level, the best-fitting halo concentrations to our post-mergers ($c = 0.76^{+1.04}_{-0.52}$) and controls ($c = 3.74^{+0.39}_{-0.34}$) can range between $[0.03, 5.30]$ and $[2.99, 4.68]$, respectively. Although previous work has shown that concentrations in post-merger systems may be lower than those of non-mergers by up to a factor of ≈ 2 (depending on how long it has been since the merger event, see Wang et al. 2020, fig. 4), our data do not provide statistically significant constraints on how mergers can affect the DM structure of galaxies.

Moreover, these best-fitting concentrations are somewhat smaller than those predicted from simulations. For instance, our concentrations are not consistent with the Duffy et al. (2008) concentration-mass relation (hereafter Duffy08), which predicts concentrations of 6.58 and 6.91 for halo masses equal to the best-fitting M_{halo} of the post-mergers and controls, respectively. These correspond to discrepancies of $\approx 2.1\sigma$ for the post-mergers and $\approx 3.2\sigma$ for the controls. One possible explanation is that Duffy08 is calibrated using dark matter only (DMO) simulations, but baryonic feedback in galaxies pushes mass out to larger radii, thereby decreasing concentrations relative to Duffy08 (Duffy et al. 2010; Shao et al. 2023).

When feedback is included, Duffy et al. (2010) show that the concentration of a galaxy’s DM component decreases by about 15 per cent compared to an equivalent DMO simulation with no feedback, so we might expect $c \approx 6.91 \times 0.85 \approx 5.87$ for the DM component. There is more to the story, however, as our lensing measurements are sensitive to not only the DM but also the gas in our samples. The mass in $M_{\text{halo}} \sim 4 \times 10^{12} M_{\odot}$ galaxies consists of ≈ 85 per cent DM, ≈ 2 per cent stars, and ≈ 13 per cent gas. It is this gas that is pushed

out to large radii by feedback, so the concentration of the combined DM and gas will be even lower than DM alone.

Table 1 also contains the SHMRs of our various datasets. By comparing the SHMRs of our post-mergers to our controls, we can determine if sustained, elevated SF occurs during the merger process that is sufficient to produce a detectable difference in their SHMRs. While the SHMRs themselves may be subject to systematic errors, the *ratio* of the SHMRs of these matched samples should be robust because systematics will affect the halo masses in the same way. Our observed ratio of the post-merger SHMR to control SHMR is $\mathcal{R} = 0.58^{+0.53}_{-0.28}$ (cf. Table 1). Using the models from Hudson et al. (2015) and the average stellar mass of the post-mergers in Table 1, our results rule out extreme (≥ 60 per cent) bursts of SF at the 95 per cent confidence level. Therefore, merger events do not, in general, yield galaxies with extreme SHMRs relative to non-mergers. Indeed, Ferreira et al. (2025) find that galaxies with $M_{\star} \sim 10^{11} M_{\odot}$ only increase their final stellar masses by ≈ 10 per cent after a merger (see also Reeves & Hudson 2024). Such a burst would predict $\mathcal{R} \sim 1.4$, consistent with our result.

To detect a starburst of similar (≈ 10 per cent) magnitude using weak lensing, we would require a sample of $\sim 15\,000$ post-mergers to reduce our observed error in \mathcal{R} to ≤ 0.2 . This is about 10 times larger than the current sample. Assuming 5 per cent of observed galaxies are merger products (Casteels et al. 2014; Ferreira et al. 2024), the full dataset would therefore need to have $\sim 300\,000$ galaxies with individual redshift measurements.

A post-merger sample of this size is most likely to come from either lenses that only have photometric, not spectroscopic, redshifts or from surveys by *Euclid* or the Dark Energy Spectroscopic Instrument (DESI). In addition to a larger post-merger sample, DESI should also be able to obtain redshifts and other measurements for galaxies that are within $55''$ of each other since its survey strategy observes the same patches of sky multiple times. This is in contrast to SDSS, where most areas in the sky are only covered by one pointing so galaxies that are too close together only have a single redshift due to fibre collisions, as in our current catalogue (also see the discussion in Section 3.1). The DESI data would therefore make our environment control more robust, since neighbouring galaxies that were previously missed are now accounted for. Finally, DESI surveys are also deeper than SDSS, which should provide lenses at a more optimal redshift for UNIONS source galaxies.

5 CONCLUSIONS

In this paper, we use galaxy-galaxy lensing to investigate how mergers change the DM haloes and stellar content of galaxies. Our lens galaxies come from a catalogue of candidate mergers taken from UNIONS and SDSS DR7, while our source galaxies come from the UNIONS ShapePipe v1.3 catalogue. To ensure differences in the lensing measurements are due to the merger process, we weight the post-mergers and non-merging control galaxies to have the same distributions of stellar mass M_{\star} , redshift z , and geometric mean distance to their three nearest neighbours R_{avg} . Additionally, we only use galaxies that live in low-density environments to reduce the effect of the 2-halo term. Our final sample consists of 1 623 post-mergers and $\approx 30\,000$ controls.

Using these data, we measure their $\Delta\Sigma$ amplitudes and find that post-mergers and non-merging controls produce similar lensing signals. We adopt a two-component model to fit to the lensing measurements below $R \leq 1.0$ Mpc consisting of a fixed point-like stellar mass contribution and an NFW halo with halo mass and concentration as

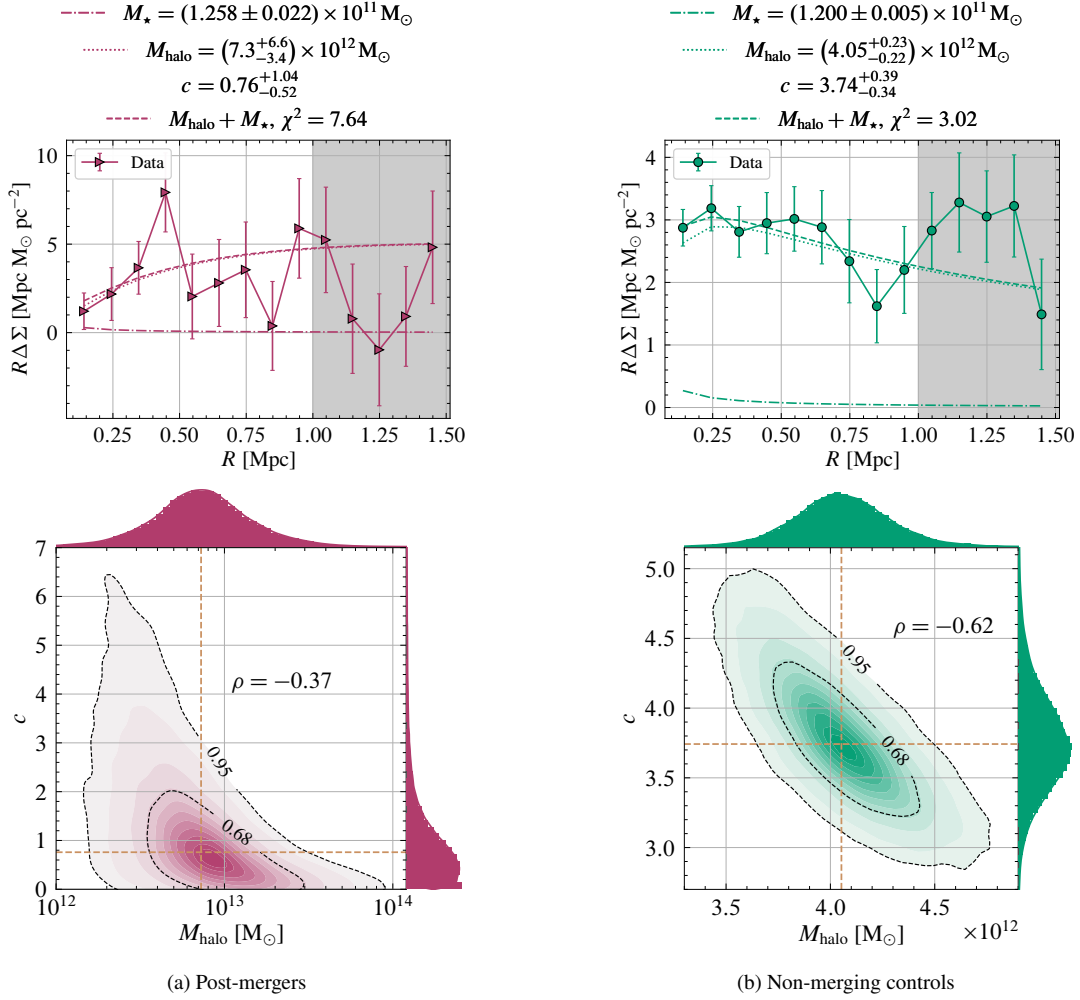


Figure 7. NFW halo fits to the lensing signal and correlations in the fitted parameters. The lower panels show the Pearson product-moment correlation coefficient ρ between the concentration c and the halo mass M_{halo} , with the 68 and 95 percentile contours indicated. The nominal (i.e. median) values of these parameters are marked with dashed gold lines. Note that the fit and all its derived parameters (including the uncertainties, χ^2 , and ρ) only consider the data points not in the shaded region, as discussed in Section 3.5.

Table 1. Summary table including number of data points N in each sample, mean redshift, parameters in our model, SHMR, and goodness-of-fit hypothesis testing results for the null hypothesis that the data and model are consistent, with 7 DoF.

Sample	N	$\langle z \rangle$	$M_{\star} (\times 10^{11} M_{\odot})$	$M_{\text{halo}} (\times 10^{12} M_{\odot})$	c	$M_{\star}/M_{\text{halo}} (\%)$	χ^2	p -value
Post-Mergers	1 623	0.1525 ± 0.0012	1.258 ± 0.022	$7.3^{+6.6}_{-3.4}$	$0.76^{+1.04}_{-0.52}$	$1.7^{+1.6}_{-0.8}$	7.64	0.37
Controls	30 048.76	0.1508 ± 0.0003	1.200 ± 0.005	$4.05^{+0.23}_{-0.22}$	$3.74^{+0.39}_{-0.34}$	$2.96^{+0.17}_{-0.16}$	3.02	0.88

free parameters. Overall, we do not find significant differences in the DM haloes of galaxies, nor in their stellar fractions, as they progress along the merger sequence. NFW haloes fitted to the two sets of lensing measurements both have $M_{\text{halo}} \sim 4 \times 10^{12} M_{\odot}$ and show moderately negative correlation between halo mass and concentration. The best-fitting post-merger concentration of $c = 0.76^{+1.04}_{-0.52}$ is not significantly different from (i.e. within 2σ of) the best-fitting $c = 3.74^{+0.39}_{-0.34}$ of the controls. These concentrations are smaller than those predicted from simulations, but this may be due to differences between feedback in nature and feedback in simulations, and/or limitations of our two-component model. We find that the post-mergers and controls have SHMRs of $1.7^{+1.6}_{-0.8}$ and $2.96^{+0.17}_{-0.16}$ per cent, respectively. This suggests

that merger events do not produce sufficient elevated SF to greatly affect the resulting SHMR of the post-merger, in agreement with previous studies.

We have shown that weak lensing is a viable method to study the properties of galaxy mergers. With a more complete dataset of merger products, or of weak lensing source galaxies, such as from DESI, Rubin/LSST, *Euclid*, and *Roman*, we may yet uncover more of the complex effects that galaxy mergers have on their progenitors using galaxy-galaxy lensing.

ACKNOWLEDGEMENTS

We are honoured and grateful for the opportunity of observing the Universe from Maunakea and Haleakala, which both have cultural, historical and natural significance in Hawaii. This work is based on data obtained as part of the Canada–France Imaging Survey, using observations obtained with MegaPrime/MegaCam, a joint project of the Canada–France–Hawaii Telescope (CFHT) and CEA Saclay, on the CFHT, which is operated by the National Research Council of Canada, the Institut National des Sciences de l’Univers of the Centre National de la Recherche Scientifique of France, and the University of Hawaii. This research is based in part on data collected at Subaru Telescope, which is operated by the National Astronomical Observatory of Japan. Pan-STARRS is a project of the Institute for Astronomy of the University of Hawaii, and is supported by the NASA SSO Near Earth Observation Program under grants 80NSSC18K0971, NNX14AM74G, NNX12AR65G, NNX13AQ47G, NNX08AR22G, 80NSSC21K1572, and by the State of Hawaii.

This research used the facilities of the Canadian Astronomy Data Centre operated by the National Research Council of Canada with the support of the Canadian Space Agency. Additionally, we are grateful for the computing resources of the Digital Research Alliance of Canada¹² and the CANFAR (Canadian Advanced Network for Astronomical Research) Science Portal¹³ for enabling the analysis in this paper.

MJH acknowledges support from NSERC through a Discovery Grant. HH is supported by a DFG Heisenberg grant (Hi 1495/5-1), the DFG Collaborative Research Center SFB1491, an ERC Consolidator Grant (No. 770935), and the DLR project 50QE2305.

DATA AVAILABILITY

The merger catalogue from Ferreira et al. (2024) is publicly available on GitHub¹⁴ with redshifts from SDSS DR7 and stellar masses from MPA-JHU (as discussed in the text).

A subset of the raw data underlying the source catalogue used in this article is publicly available via the Canadian Astronomy Data Centre¹⁵. The remaining raw data and all processed data are available to members of the Canadian and French communities via reasonable requests to the principal investigators of the Canada–France Imaging Survey, Alan McConnachie and Jean-Charles Cuillandre. All data will be publicly available to the international community at the end of the proprietary period.

REFERENCES

Bertin E., 2011, in Evans I. N., Accomazzi A., Mink D. J., Rots A. H., eds, *Astronomical Society of the Pacific Conference Series Vol. 442, Astronomical Data Analysis Software and Systems XX*. p. 435

Bertin E., Arnouts S., 1996, *A&AS*, **117**, 393

Bickley R. W., et al., 2021, *MNRAS*, **504**, 372

Bruzual G., Charlot S., 2003, *MNRAS*, **344**, 1000

Bryan G. L., Norman M. L., 1998, *ApJ*, **495**, 80

Casteels K. R. V., et al., 2014, *MNRAS*, **445**, 1157

Chabrier G., 2003, *PASP*, **115**, 763

Cooray A., Sheth R., 2002, *Phys. Rep.*, **372**, 1

¹² <https://ccdb.alliancecan.ca/>

¹³ <https://www.canfar.net/science-portal/>

¹⁴ https://github.com/astroferreira/MUMMI_UNIONS

¹⁵ <http://www.cadc-ccda.hia-ihp.nrc-cnrc.gc.ca/en/megapipe/>

Davies J. J., Pontzen A., Crain R. A., 2022, *MNRAS*, **515**, 1430

Desai S., et al., 2012, *ApJ*, **757**, 83

Diemer B., 2018, *ApJS*, **239**, 35

Domingue D. L., Xu C. K., Jarrett T. H., Cheng Y., 2009, *ApJ*, **695**, 1559

Duc P. A., Brinks E., Wink J. E., Mirabel I. F., 1997, *A&A*, **326**, 537

Duffy A. R., Schaye J., Kay S. T., Dalla Vecchia C., 2008, *MNRAS*, **390**, L64

Duffy A. R., Schaye J., Kay S. T., Dalla Vecchia C., Battye R. A., Booth C. M., 2010, *MNRAS*, **405**, 2161

Ellison S. L., Patton D. R., Simard L., McConnachie A. W., 2008, *AJ*, **135**, 1877

Ellison S. L., Mendel J. T., Patton D. R., Scudder J. M., 2013, *MNRAS*, **435**, 3627

Ellison S. L., et al., 2022, *MNRAS*, **517**, L92

Ellison S., Ferreira L., Wild V., Wilkinson S., Rowlands K., Patton D. R., 2024, *The Open Journal of Astrophysics*, **7**, 121

Farrens S., et al., 2022, *A&A*, **664**, A141

Ferreira L., et al., 2024, *MNRAS*, **533**, 2547

Ferreira L., Ellison S. L., Patton D. R., Byrne-Mamahit S., Wilkinson S., Bickley R., Conselice C. J., Bottrell C., 2025, *MNRAS*, **538**, L31

Gonzalez E. J., et al., 2023, *MNRAS*, **522**, 5655

Guinot A., et al., 2022, *A&A*, **666**, A162

Hartlap J., Simon P., Schneider P., 2007, *A&A*, **464**, 399

Harvey D., Courbin F., 2015, *MNRAS*, **451**, L95

Heymans C., et al., 2012, *MNRAS*, **427**, 146

Hildebrandt H., et al., 2012, *MNRAS*, **421**, 2355

Hopkins P. F., Hernquist L., Cox T. J., Di Matteo T., Robertson B., Springel V., 2006, *ApJS*, **163**, 1

Hudson M. J., et al., 2015, *MNRAS*, **447**, 298

Huertas-Company M., et al., 2015, *ApJS*, **221**, 8

Huff E., Mandelbaum R., 2017, *arXiv e-prints*, p. [arXiv:1702.02600](https://arxiv.org/abs/1702.02600)

Jogee S., et al., 2009, *ApJ*, **697**, 1971

Kado-Fong E., Robinson A., Nyland K., Greene J. E., Suess K. A., Stierwalt S., Beaton R., 2024, *ApJ*, **963**, 37

Kauffmann G., et al., 2003, *MNRAS*, **341**, 33

Kish L., 1992, *Journal of Official Statistics*, **8**, 183

Knapen J. H., Cisternas M., Querejeta M., 2015, *MNRAS*, **454**, 1742

Kohonen T., 1982, *Biological Cybernetics*, **43**, 59

Lange J., Huang S., 2022, *DSIGMA: Galaxy-galaxy lensing Python package, Astrophysics Source Code Library, record ascl:2204.006*

Li Q., et al., 2024, *ApJ*, **969**, L25

Liaudat T., Bonnin J., Starck J. L., Schmitz M. A., Guinot A., Kilbinger M., Gwyn S. D. J., 2021, *A&A*, **646**, A27

Mohr J. J., et al., 2012, in *Software and Cyberinfrastructure for Astronomy II*. pp 121–132

Moreno J., et al., 2019, *MNRAS*, **485**, 1320

Nelson D., et al., 2019, *Computational Astrophysics and Cosmology*, **6**, 2

Patton D. R., Atfield J. E., 2008, *ApJ*, **685**, 235

Patton D. R., Faria L., Hani M. H., Torrey P., Ellison S. L., Thakur S. D., Westlake R. I., 2024, *MNRAS*, **529**, 1493

Pearson W. J., Wang L., Trayford J. W., Petrillo C. E., van der Tak F. F. S., 2019a, *A&A*, **626**, A49

Pearson W. J., et al., 2019b, *A&A*, **631**, A51

Prat J., et al., 2022, *Phys. Rev. D*, **105**, 083528

Reeves A. M. M., Hudson M. J., 2024, *MNRAS*, **527**, 2037

Robaina A. R., et al., 2009, *ApJ*, **704**, 324

Rose C., et al., 2024, *ApJ*, **976**, L8

Sanders D. B., Soifer B. T., Elias J. H., Madore B. F., Matthews K., Neugebauer G., Scoville N. Z., 1988, *ApJ*, **325**, 74

Shah E. A., et al., 2022, *ApJ*, **940**, 4

Shao M. J., Anbajagane D., Chang C., 2023, *MNRAS*, **523**, 3258

Springel V., Di Matteo T., Hernquist L., 2005, *MNRAS*, **361**, 776

Strauss M. A., et al., 2002, *AJ*, **124**, 1810

Tago E., Saar E., Tempel E., Einasto J., Einasto M., Nurmi P., Heinämäki P., 2010, *A&A*, **514**, A102

Wang K., Mao Y.-Y., Zentner A. R., Lange J. U., van den Bosch F. C., Wechsler R. H., 2020, *MNRAS*, **498**, 4450

Wilkinson S., Ellison S. L., Bottrell C., Bickley R. W., Byrne-Mamahit S., Ferreira L., Patton D. R., 2024, *MNRAS*, **528**, 5558

Wright A. H., Hildebrandt H., van den Busch J. L., Heymans C., 2020, *A&A*, 637, A100
Xu C. K., Zhao Y., Scoville N., Capak P., Drory N., Gao Y., 2012, *ApJ*, 747, 85

Zuntz J., et al., 2018, *MNRAS*, 481, 1149

This paper has been typeset from a \TeX/L\TeX file prepared by the author.